Performance uniformity analysis in polymer electrolyte fuel cell using long-term dynamic simulation

S. Culubret [a], M.A. Rubio [b,*], D.G. Sanchez [c], A. Urquia [b]

[a] Escuela Internacional de Doctorado, Programa de Ingeniería de Sistemas y de Control, Universidad Nacional de Educación a Distancia (UNED), Spain
[b] Departamento de Informática y Automática, Universidad Nacional de Educación a Distancia (UNED), Spain
[c] Institute of Engineering Thermodynamics, Deutsches Zentrum fur Luft und Raumfahrt (DLR), 70569 Stuttgart, Germany

ARTICLE INFO

ABSTRACT

The temporal stability and spatial homogeneity of current density are key factors in Polymer Electrolyte Fuel Cell (PEFC) performance and durability. Temporal and spatial variations of relative humidity, fuel concentration, and water droplets in the channels are the principal causes of non-homogeneous current density. A dynamic pseudo-3D model was previously proposed by the authors and has been extended and improved to perform the long-term and intensive simulations of PEFC with low computational cost, which allows to study of the performances homogeneity with different experimental configurations and flow field topologies. The model considers important phenomena in the homogeneity analysis, such as gases and liquid water movement in diffusion layers and flow field, electrochemical reactions, and others. Model validation has been performed using experimental data obtained from a 25 cm^2 cell with a single serpentine, which has allowed studying the model transient response and spatial representation. The simulations have been used to study the homogeneity and stability of 36 setups of PEFC, varying the rib/channel width ratio, the stoichiometric ratio, and the number of parallel serpentine channels. The results show the importance of a properly flow field design to control gas flow, remove the channels' liquid water, and keep a homogeneous feeding. The study evaluated a set of channel configurations that show the improved temporal voltage stability and current density spatial homogeneity. The results show the impact of channel gas speed and ratio channel/rib width in liquid droplets removal and the proper fuel spatial distribution; and how configurations with a lesser number of channels in serpentine design require a lower stoichiometric ratio to perform better temporal and spatial uniformity. In the case of the cell configurations simulated, the optimum design was achieved using between 5 and 7 parallel serpentine channels and a channel/rib ratio 3/5.

1. Introduction

Energy production, especially in transport, is based on fossil fuels, and their sub-products (mainly CO_2) are responsible for global warming. Climate change effects are driving initiatives worldwide, such as COP26 [1], to set goals to reduce emissions by 2030 and reach a net-zero emission target by 2050. The hydrogen society is a complete energy model and is postulated as one of the paradigms for meeting these objectives, in which PEFCs are fundamental elements. Significant research efforts are being carried out to achieve the challenges of this technology for commercial implementation. Typically, PEFC provides an efficiency of 60%. The energy losses manifest as heat in some systems, and it can be used in the co-generation cycle, increasing efficiency up to 80%.

Studying the durability and robustness of PEFCs is a very active research area. Temporal variation or non-uniform working conditions negatively impact the lifetime of components. Improper water management in the cell produces inhomogeneity in its performance. Also, non-uniform evaporation and condensation, liquid water moving, or gases with different relative humidity along the cell produce variations in current densities or voltage [2].

Flow field design is crucial in water management and proper gas distribution and, therefore, in PEFC's performance. Some studies have analyzed the impact of water management and gas concentration on the fuel cell homogeneity and stability. Variations of channel height and width in straight channels have been studied to understand the impact on local current density [3], as well as the effect of channel–rib

Nomenclature

ϵ	Porosity
ϵ	Surface tension ($N \cdot m^{-1}$)
γ	Interface tension (Nm^{-1})
κ	Permeability ($m^{-2} \cdot$)
λ	water content in ionomer membranes ratio water and sulfonic acid groups molecules
μ	Dynamic viscosity ($Pa \cdot s$)
ρ	Density of the fluid ($kg \cdot m^{-3}$)
ρ	Density of the liquid ($kg \cdot m^3$)
τ	Porous medium tortuosity
θ	Contact angle (rad)
e_r	Relative roughness of the duct
Re	Reynolds number
$\dot{w}_a$	Water flow during the re-absorption ($mm^3 \cdot s^{-1}$)
σ_m	Electric conductivity of the membrane ($S \cdot cm$)
A	Area (m^2)
A_d	Cross-section area of the droplet perpendicular to the advancing axis (m^2)
C_d	Aerodynamic coefficient of the droplet
c_t	Compressibility of the fluid plus the compressibility of the GDL
$C_{O_2,0}$	Reference O_2 concentration
$C_{O_2,0}$	Reference O_2 concentration
D_d	Diameter of the droplet (m)
D_h	Hydraulic diameter (m)
$D_{i,j}$	Binary diffusion among substance i and j ($m^2 \cdot s$)
E_{oc}	Reversible open-circuit potential (V)
F	Faraday constant ($s \cdot A \cdot mol^{-1}$)
F_{drag}	Droplet gas dragging force (N)
h_d	droplet height (m)
IEC	Ionic exchange capacity (m)
j	Current density ($[A \cdot cm^{-2}]$)
J_i	Molar diffusive flux ($mol \cdot s^{-1}$)
j_0	Exchange current density ($A \cdot cm^{-2}$)
k	Evaporation/condensation constant ($[Pa^{-1} \cdot s^{-1}]$ and $[s^{-1}]$)
k_{adh}	Constant adhesion force function of droplet shape
L	Length (m)
M	Molar mass ($kg \cdot mol^{-1}$)
m	mass (g)
P	Pressure (Pa)
R	Gases constant ($J \cdot K^{-1} \cdot mol^{-1}$)
R	Radius (m)
R_d	Radius of the droplet (m)
s	Water content in the porous media
T	Temperature (K)
t_d	Droplet contact line (m)
th	Thickness (m)
th_m	Thickness (m)
V	Volume (m^3)
V_{act}	Activation overvoltage (V)
V_{con}	Concentration overvoltage (V)
V_{ohm}	Ohmic overvoltage (V)
w_d	Droplet width (m)
WU	Water uptake (m)
x	Length (m)
A	Advancing
bd	Back diffusion
cap	Capillary
con	Condensation constant from porous media
eo	Electro-osmotic
evp	Evaporation constant from porous media
g	Gas
liq	Liquid
n_d	Electro-osmotic drag coefficient ($mol_{H_2O} \ mol_{H^+}^{-1}$)
R	Receding
S	Static
sat	Saturation state

ratio using a 2D model [4]. The improvement of liquid water removal using a flow field design with micro-channels has been analyzed in [5].

The effect of gas flow on water accumulation inside the channel with counter and co-flow configuration [6], and considering the gravity, was studied [7,8]. The effect of the pressure drop in the channels in function of different gas flows quantity [9,10] also focus on improving cell performance homogeneity. The impact of the spatial homogeneity, the time stability of relative humidity (RH), and liquid water content in the cell's durability are analyzed in drying conditions using 300 cm^2 cell [11].

Water content in the cell can be controlled by modifying the inlet gases' RH. The reactant consumption and the increasing of RH along the channels are critical phenomena in the cell's performance. This effect is especially relevant in long channels since the relative pressure of reactants plays a crucial role in the local performance of the cell. The gradient of RH along the channels has been analyzed using model simulation in multiple studies. The impact of RH along a single straight channel and its impact on the cell performance has been studied in [12]. Single straight are also used to study the RH evolution for different channel designs [13].

Fuel Cell durability has been widely studied by analyzing the effects of different component materials and experimental setups. The effect of cold starts on membrane electrode assembly (MEA) durability has been studied in [14] Also, the cracks in the microporous layer (MPL) consequence of the liquid water removal have been analyzed in [15].

Mechanical failures in the cell negatively affect its performance and have been extensively studied. The mechanical stress on thin membranes exposed to differential pressure can cause membrane breakage [16]. The mechanical stresses in the gas diffusion layer (GDL) have been analyzed using a 2D model in [17]. The impact of RH and temperature on the membrane tensile strength, which reduces its durability, has been studied in [18,19].

Also, a non-homogeneous consumption of O_2 or H_2, gases distribution in the flow field, variation of RH, or amount of liquid water along the channels produce uneven aging of the cell, which leads to uneven degradation [20].

Adequately stoichiometry is crucial for the homogeneity of gas concentration in the active area. The balance between stoichiometry and gas flow is fundamental to maintaining an appropriate amount of liquid water while keeping the cell performance uniform, minimizing fuel consumption [21].

Relating those results with the durability and degradation studies [22–24], the spatial homogeneity and stability reduce the uneven performance, which leads to cell degradation.

Due to the complexity of multiphysics phenomena in fuel cells, it is necessary to use analytical tools to understand the effect of design and operating parameters on performance, allowing to optimize their efficiency and improve their robustness and durability. The physical

modeling of fuel cells is a valuable tool to optimize the design and the election of accurate physical and operating parameters. This tool allows a systematic evaluation to be carried out when the experimental procedure is not available or the economic cost is significant. Fuel cell models have been oriented for different purposes and to varying levels of complexity. Typically the studies in PEFCs have been focused on modeling three components: the GDL, the membrane layer, and the flow field. The models can be classified by the capability to represent the time evolution of variables as dynamic or steady-state. Steady-state models have been used to study the impact of RH variation along the channel [12], or the fuel concentration evolution below the rib in a 2D model [17]. Most of the steady-state models consider that the electrochemical reactions are faster than the rest of the phenomena occurring in the cell, such as water or gas diffusion [25]. The dimensionality of the models developed to study the PEFC varies from 0D to 3D models. The 0D models do not consider dimensionality, such as those that represent the electrical behavior of the cell (I–V response) using a set of analytical equations. The 1D models are typically used to study the phenomena perpendicular to the MEA plane, such as the water distribution and gas concentration inside the MEA [26]. 2D PEFC models are widely used to study the spatial effect of flow field design, reactants distribution, and humidity dynamic evolution [17,27]. Finally, 3D models are those which take into account all spatial dimensions coupled simultaneously [28]. Typically the simulation of those models has a high computational cost. The complexity of the 3D models may vary from single straight channels with half rib at each side of the cell to the study of gases and liquid water concentration distribution in the complete cell. Also, different dimensional representation in the model is possible, such as 1D+1D or 1D+2D. An example of a pseudo-2D model is presented in [29] which combines a 1D cathode CL model and a 1D flow field model to simulate the time evolution of species in a 2D plane. More complex models are used in [30] where a pseudo-3D model is developed using a combination of plane 2D models of MEA layers coupled with a 3D channel model to represent a 3D fuel cell with a single channel. To study water management in a fuel cell stack, a 2D+1D model was used in [31]. This model used a 2D plane model to represent CL, membrane, and GDL, and 1D models to connect each 2D sub-model. The result is a pseudo-3D model even the 3 dimensions are not coupled. The number of dimensions used in a model is related to the phenomena to be represented and affects the computational effort of simulations. This pseudo-3D modeling approach is similar to the modeling methodology employed in this paper.

The modeling and simulation process to study the optimization of PEFC performance requires intensive simulation to analyze the effect of many operational and design parameters. The computational effort in simulations plays a fundamental role if a large number of experimental simulations have to be conducted since some complex model simulations can take many hours or even days. This constraint makes the usability of parametric analysis impracticable. A multi-dimensional representation model approach is used in this work since the aim is to optimize the computational effort of the simulations while maintaining the accuracy of the results obtained. The model presented in this work is a pseudo-3D model composed of 2D models representing the GDLs, 1D for membrane, pseudo-3D for flow fields, pseudo-3D for water droplet movement, 0D for electrochemical reactions and 0D for evaporation/condensation in the GDLs, and flow fields. The fuel cell model presented allows representing the dynamic behavior due to changes or instability in cell operating conditions.

The GDL has been modeled with different objectives such as understanding the water distribution [32] and how it is affecting the access of gases into the catalyst layer, especially under the ribs. The effect of GDL aging on water management has been studied in [33]. Other models evaluate the surface treatments on the GDL to accelerate the liquid water removal from the GDL to the channel [34] or the diffusion of gases inside the GDL [35,36]. The consumption of fuel and the concentrations under the rib are studied in [37].

Regarding the membrane layer model (MLM), some studies are focused on the electrolyte conductivity [38]. The conductivity and water diffusion coefficients have to been estimated and adjusted in [39]. These coefficients vary due to fabrication variability and aging of the electrolyte.

The investigations using gas flow field models are oriented in channel topologies analysis. In [40] studied the serpentine-shaped channels and the impact of the corner design on the gas flow distribution. Also, the pressure drop was studied, analyzing the channel/rib ratio and its effect on the power density [27,41]. Other studies focused on water removal and uniform fuel distribution [5,27].

The movement of droplets inside a channel under certain conditions has been calculated analytically in [42,43] and numerically in [40], using VOF (Volume of Fluid) method. Also, a complex simulations approach of water split and dragging, based on micro-scale model description, is analyzed in [44]. This numerical method allows to simulate highly complex models, considering the water and gas mixture and provides very accurate results, but high-performance hardware and huge computational effort are required. Analytical methods are much faster but require the adoption of many modeling approaches that reduce the flexibility of their use.

One of the problems of performing long-term fluid-dynamic model simulations, which aim to represent two phases (liquid and gaseous) of water, with the rest of the gas species involved, is the required computational effort [45]. Most of the previous fluid-dynamic models show accurate results; however, the complexity of the models representing the phenomena studied does not allow for intensive and long-term simulations due to high computational cost. Model simplification strategies were evaluated to allow long-term simulations. In [46] a system order simplification was used in fuel cell control modeling. Much more complex models have been already developed, such as [47,48], in these cases, 3D stack model has been simulated, and each solution converged after around 24 hours with more computing capabilities.

In this paper, new modeling and simulation strategies have been developed to improve the computation time without compromising the accuracy of the results. The model presented is an enhanced extension of the model shown by the authors in [49]. The model has been improved in 5 different aspects: (a) a model of water droplet reabsorption into GDL from the channels is included; (b) an improved model of membrane conductivity is added to better fitting to the fuel cell performance; (c) a new model of water droplet movement in the channel to optimize the duration of the simulation time is included; (d) non-uniform spatial discretization grid is used to improve the accuracy of the simulations when applying the different flow field geometries; and (e) some submodels have been implemented in C++ language to reduce computational simulation time, which has been reduced up to 50%.

Experimental validation of the model has been carried out, evaluating its capacity to represent the dynamic behavior under different experimental conditions. In addition, simulations of the model have been conducted to study the effect on the homogeneity of gas distribution, current density, and water content as a function of different flow field setups. The high homogeneity of these variables may improve the durability and robustness of the cell.

The article is structured in the following parts. First, in Section 2, a review of the model and a brief description of the new functionalities are explained. In Section 3 the characteristics and the steps followed in the simulation procedure are presented; following Section 4, where the experimental validation is performed using dynamic experimental data. The experimental validation is focused on evaluating the model's capabilities to represent spatial and dynamic performance.

Section 5 shows an analysis of the effect of different flow-field design parameters on the homogeneity and stability of the cell variables by performing long-term simulations. The impact of the number of parallel channels, rib–channel ratio, and stoichiometry are evaluated. In addition, the parallel straight channels design and its effect is analyzed. The computational performance of the simulations are shown in Section 6. Finally, Section 7 presents the main highlights of the investigation.

2. Model development

The model presented in this paper is an extension of the previously shown in [49]. The complete model's equations are presented in Appendix A, and it is focused on the dynamic performance impact related to water distribution in the cell.

This section shows the main novelties included in the described physical phenomena of the model: the re-humidification of the GDL due to the presence of liquid water on the surface of the GDL, an improved membrane conductivity model, and a droplet movement model simplification.

The improvements in the simulation procedure are presented in Section 3: discretization strategy and implementation of some computational high-cost submodels in C++ to improve the computation time.

The model is an isothermal pseudo-3D model composed of (a) pseudo-2D channel model based on a 1D channel model where the pressure drop, the fuel consumption, the RH variations, and the droplets advance are considered; (b) 2D GDL model where water and gases diffusion in the XY axes are considered; (c) one-to-one element water balance between the GDL and channel in terms of liquid water, evaporation, condensation, and fuel feeding; (d) 0D electrochemical model to evaluate the electric current and water production; and finally (e) the water balance between the cathode and anode GDLs considering electro-osmotic drag and back diffusion.

The effect of temperature can strongly influence cell behavior. In this work, the isothermal approximation of the model is appropriate to represent cell-level behavior. In the case of a stack-level study, where thermal gradients are often significant, a non-isothermal model approximation may be adequate.

Each submodel is standalone and executed sequentially to simulate the overall cell's model. The dynamic representation of the models allows the simulation of transient behaviors due to changes in the state of humidification, fuel feeding, or the presence of liquid water in the form of droplets.

2.1. Liquid water re-absorption into the GDL

The presence of liquid water over the surface of the GDL increases locally the RH, which causes steam reabsorption when the overall water content, steam, and liquid in the GDL is low. The drying effect on the anode's GDL is more common than on the cathode due to the electro-osmotic drag effect and water production at the cathode. The water uptaking of hydrophobically treated GDL from the flow field is an asymmetric process since liquid water is more easily expelled from the GDL than absorbed.

The water re-absorption process depends mainly on the droplet size over the surface and the water content inside the GDL. The re-absorption flow is calculated at each time step while the droplet advances. The uptaken water amount is calculated considering the average GDL water content along the droplet path. The submodel description is detailed in Appendix A.1.4.

Due to the water flow during the re-absorption, the droplet volume is reduced during its advance in the channel. The liquid water re-absorption quantities are small compared with the droplet volumes (around 2 to 3% of the droplet volume per second in our simulations). Therefore, the droplet volume is considered constant during each time iteration in a small-time interval. This simplification enables less frequent updating of the droplet volume value during the simulation.

2.2. Droplet movement simplification

Droplet dynamics are analyzed in [42,43,50,51]. In those studies, semi-analytic models of the droplet movement over a GDL surface are
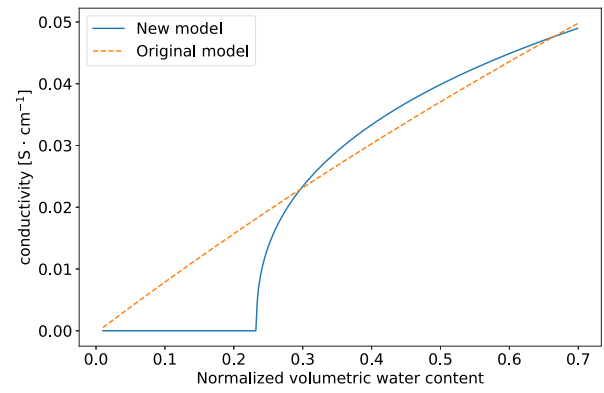

Fig. 1. Dependency of membrane conductivity on its water content, obtained simulating the previous [46] and new models.

described. In these flow field geometric models, the deformation of the droplet is taken into account to calculate the adhesion and dragging force under the action of a gas flow.

When a droplet is exposed to a gas flow it is deformed, changing its mass center and the angles with respect to the surface (advancing and receding angles). The result of the adhesion force, resistance to the advance, and drag force produce the droplet advance, which depends on the droplet's volume. It can be calculated from the geometrical model of the droplet, Appendix A.4.

Model simplification has been applied to improve the simulation time, to avoid solving the geometric model iteratively at each simulation step to compute the adhesion force. An approximation of the geometrical force function of the gas speed and the droplet speed is used, which turns the droplet speed into a first-order system.

2.3. Membrane conductivity

The ohmic resistance overvoltage is an important effect in the cell performance. It defines the linear component of the polarization curve in the typical operating range.

The membrane conductivity, σ_m, depends on its humidification, calculated based on the water activity [49]. In the model presented in this paper, the water content in the membrane is calculated using the water uptake (W_U), and the ion exchange capacity [38]. The conductivity model used is represented by Eq. (1), where σ_0 is the reference membrane conductivity, and W_{U_c} is a water threshold uptake.

$$\sigma_m = \begin{cases} 0 & \text{, if } W_U < W_{U_c} \\ \sigma_0 \left(W_U - W_{U_c} \right)^\beta & \text{, if } W_U \geq W_{U_c} \end{cases} \quad (1)$$

In the previous model [49], based on [52], the conductivity decreases with the normalized water volume content. The model applied in this work represents more accurately the activation process of the dry membrane when it is hydrated. The comparison of the models is shown in Fig. 1. The formulae are described in more detail in Appendix A.5.

The study of the uneven distribution of protons in the through-plane direction is not studied in this work since this analysis would imply a high computational cost, compromising the balance between obtaining accurate results and simulation time.

3. Model simulation procedure

Simulating the 2D GDL model and the one-to-one connection between anode and cathode elements is highly expensive computationally. This disadvantage is significant when the number of discretization elements is considerable. This submodel has been implemented in C++

Table 1
Parameters used on the experimental simulations.

Parameter	Description	Value
d_t [s]	Simulation time step	0.5
d_x [mm]	Spatial discretization length	1
w_c [mm]	Channel width	1
H_c [mm]	Channel height	1
L_c [mm]	Channel length	47
PEFC $X \cdot Y$ [mm]	Cell size	50·50
N_{ch} [−]	Number of channels	1
$HR_{c,a}$ [%]	Anode and cathode HR range	100–6
θ_s [deg]	Contact angle	130

to reduce the simulation time. The Fig. B.15 (shown in Appendix B) represents the different sub-models and in which order they are executed. The red-dotted box (MEA Solver) marks the simulation procedure that has been implemented in the C++ language. The C++ language has been used in the model of species diffusion of the GDL. This procedure iteratively calculates the polarization curve since these stages involve a more significant computational effort than the other simulation stages. For instance, a 10×10 cm cell size, 0.125 mm element size, is divided in 640000 spatial elements. The bisection method is used to calculate all element voltages in galvanostatic mode, which implies a large number of iterations. The rest of the submodels have been implemented in Python since it allows efficient editing, modifying, and reusing.

In the model simulation procedure, the discretization area of the MEA is significantly smaller than that of the flow field (regions). For species exchange simulation at the flow field–MEA interface, the mesh size of the GDL must be an integer multiple of the flow field mesh. In the previously presented model, the flow field discretization was of fixed size, forcing the equal width of rib and channel. In the new simulations, a non-uniform mesh can be applied, giving more flexibility to use more complex flow field designs.

4. Model experimental validation

4.1. Experimental data and simulation

The developed model allows to simulate the dynamic behavior of a cell and evaluate the water content in both phases at the anode and cathode with a low computational effort. The transient dynamics of behavior of drying–humidifying showed in the experimental work [53] were used to validate the model. The experimental set contains a combination of dynamical phenomena related to water management and its impact on the cell current density, which are suitable to validate the model performance. The experimental results [53] show localized presence of water, observed using neutron imaging techniques, and the overall current density of the cell for different time steps of the experimentation.

The experiments were conducted in a 5×5 cm^2 cell. The experiments start when the cell achieves a steady state with 100% RH both in the cathode and anode. Once the steady state is reached, the RH of the anode is dropped to 6% for 400 s. From the steady state, the cell reduces its performance as it dries, reaching a lower-performing state. After that, 40 μl of liquid water is inserted during 5 s in the anode side. The conditions are maintained for another 500 s until the new insertion of liquid water and the process is repeated. During the droplet insertion, the cell is re-humidified and reaches a high-performance state. The cell configuration parameters are shown on the Table 1.

The membrane parameters used to validate the model are obtained from [54]. The membrane thickness is 27.5 μm with a specific weight of 55 g·cm^{-2} and a conductivity higher than 50.5 mS·cm^{-1} and 72.0 mS·cm^{-1}, through plane and in-plane, respectively.

In Fig. 2, a spatial comparison of the experimental and simulation results of water content and the current density is shown.

The water content in simulation and experimentation represents the total amount of water in the cell in-plane. Fig. 3 shows the comparison of simulation and experimental the transient of overall current density. The simulation results show a good fit to the experimental data, both dynamically and spatially, regarding water in the cell and current density. The error in water amount between experimental and simulation is lower than 5% (Fig. 2), and the coefficient of determination, R^2, of the current density within the time interval (0–150 s) is 88.6%, with 1 s interval sampling (Fig. 3).

The GDLs models have been discretized through the plane, which provides valuable information on the sectional behavior of the variables. In Fig. 4a, the water content in 10 s after the droplet insertion of the simulation experiment is shown in the three spatial axes. Fig. 4 also shows the water contribution of the anode and cathode's GDLs and flow fields. The spatial distribution of water in the anode and cathode GDLs and in the anode flow field is illustrated in Fig. 4b. The data shown in Figs. 4a and b are referred to the experimental simulation time of 10 s, marked with a blue marker in Fig. 3.

In Fig. 4b is shown a time delay between the highest value of water content in the cathode GDL and the maximum water peak in the anode GDL. This phenomenon is a consequence of the diffusion of water dynamics between the anode and cathode sides. The figure illustrates the presence of liquid water in the anode flow field but not in the cathode. The results of the simulation show how the liquid water injected into the anode flow field is rapidly absorbed, in the steam phase, due to the low hydration level in the anode GDL. The electro-osmotic drag keeps the anode dry enough to continue absorbing water and increasing the hydration level of both sides.

Fig. 5a shows the dynamic simulation of water content in the anode and cathode GDLs. In Fig. 5b, the electro-osmotic drag and the back-diffusion contributions as well as the overall water transferred are presented. The positive value represents the water flow in the direction from the anode to the cathode. During the hydration phase (0–30 s), the water flow to the cathode GDL increases until the anode flow field droplets are removed from the cell since the back-diffusion compensates for the water content difference until the drying phase is reached again.

The RH in the anode is kept to 100% during all the simulations, and therefore no evaporation occurs. In the GDL, accumulated water due to the absorption of liquid water droplets is solely removed via diffusion to the cathode and evaporation on the cathode side. The absorbed water in the anode crosses the membrane to the cathode due to the electro-osmotic phenomenon. The portion of water, not absorbed in steam phase into the GDL, remanent in the droplets is removed, still in liquid form, as a consequence of the gas flow in the channels.

5. Results of the spatial homogeneity and stability study

Temporal stability and spatial homogeneity of cell performance can have an incidence on the durability of the cells. In this section, the impact of different values of model parameters on the performance uniformity of the cell is analyzed. Long-term simulations have been conducted to evaluate the stability and homogeneity. Relevant statistical information on the dynamic behavior of the results can be obtained. The large number of long-term simulations performed in this study was possible due to the optimization of the model simulation time.

Configurations of parallel serpentine channels, with an area of around 10×10 cm, are simulated in Section 5.1. The main model parameters studied are (a) the channel–rib (C–R) width ratio, (b) the number of channels in the flow field, and (c) the stoichiometry ratio used in the cell. The C–R ratio and the channel number were chosen as experimental factors because they have a significant role in gas feeding and water evacuation. The stoichiometry ratio is studied to evaluate the impact of different fuel consumption for the same cell design.

The results obtained with the serpentine channel cells are compared with the parallel channel configuration in Section 5.2.
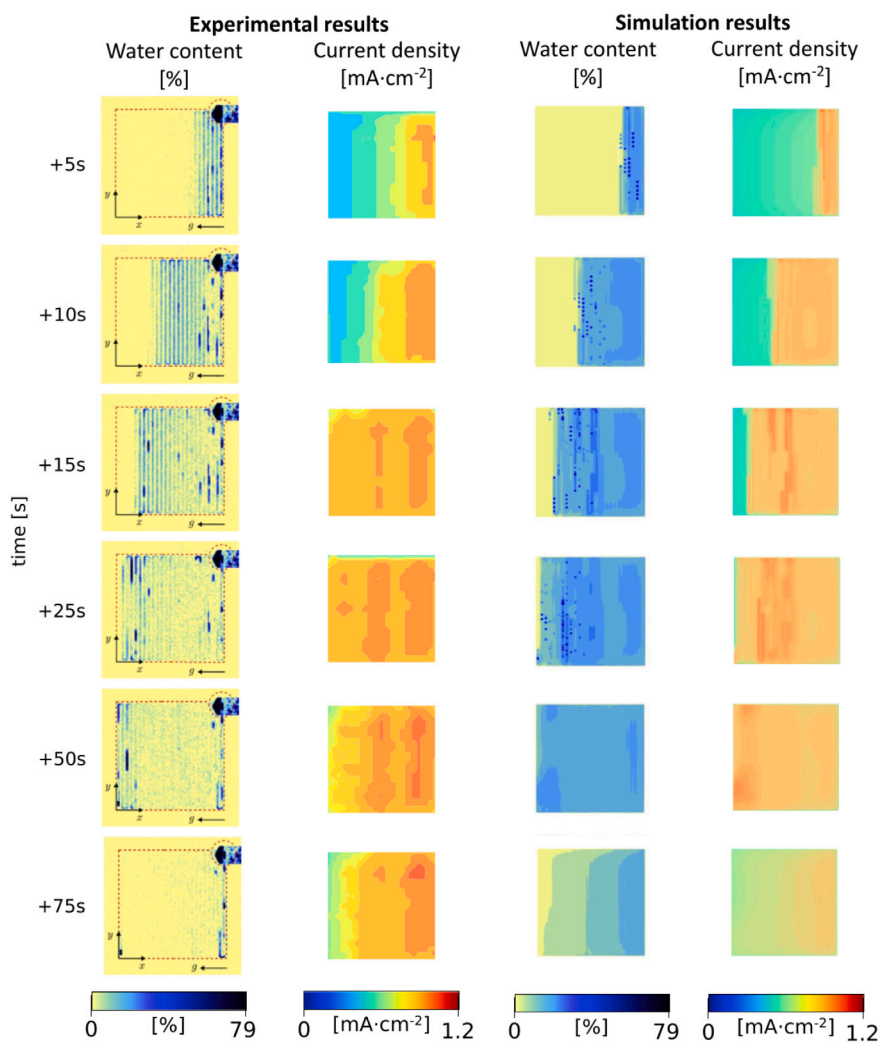
Fig. 2. Experimental and simulation results of spatial water content and current density.
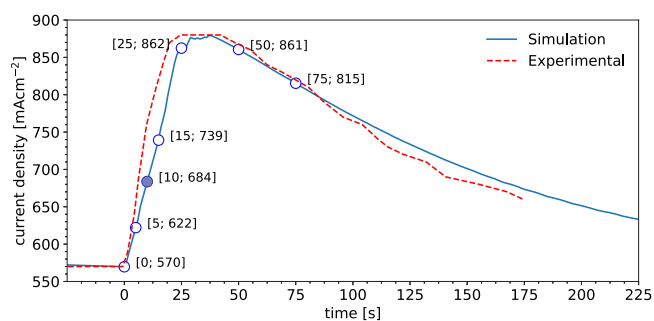

Fig. 3. Dynamic behavior of the overall current density of the cell in experimental and simulation. A filled blue marker used to reference the experimental point in Fig. 4.

The simulations are performed in a constant current mode, 0.7 A·cm^{-2} and at 80 °C operating temperature. The cell voltage is set around 0.6 V to operate around the maximum power point. The RH in cathode and anode of those simulations is 50% since the humidification becomes stable over ranges of 40% [55]. The applied gas pressure is 0.5 bar overpressure.

All the cell experimental setups are polarized in a similar power density, therefore the stability and homogeneity results are evaluated in similar performing states of the cells. The effect of current density

and temperature on water management is very relevant. This study is focused on analyzing a single operating point of constant current density and temperature. The inclusion of new study parameters in the simulation experimental matrix would make the analysis of the results more complex and significantly increase the number of simulations to be conducted.

Two properties have been considered to analyze the uniformity of the cell performance: (a) temporal stability and (b) spatial homogeneity in XY plane. All the simulations, except the unstable ones, are 1000 s length (16 min. approximately) which is considered enough to evaluate non-homogeneities or cell stability for a constant current demand. The temporal analysis of these values is evaluated only within the interval 250 s–1000 s to reduce any transient stabilization effect. Each simulated configuration has been studied in the following two ways: (a) spatial analysis to evaluate the average and the standard deviation of the current density; and (b) temporal analysis to calculate the average and standard deviation of the voltage and the overall current along time window (250 s–1000 s).

The spatial average of the variable x at the time step t, $\overline{x_t^h}$, is calculated using Eq. (2), where n_p is the total number of spatial discretized elements in XY plane. The spatial standard deviation of variable x_t^h, $\sigma_{x_t}^h$, is calculated by using Eq. (3). The values obtained depend on the spatial discretization size. In this work, the spatial measurements are done every 5 mm in both axes. Therefore, a cell will typically contain
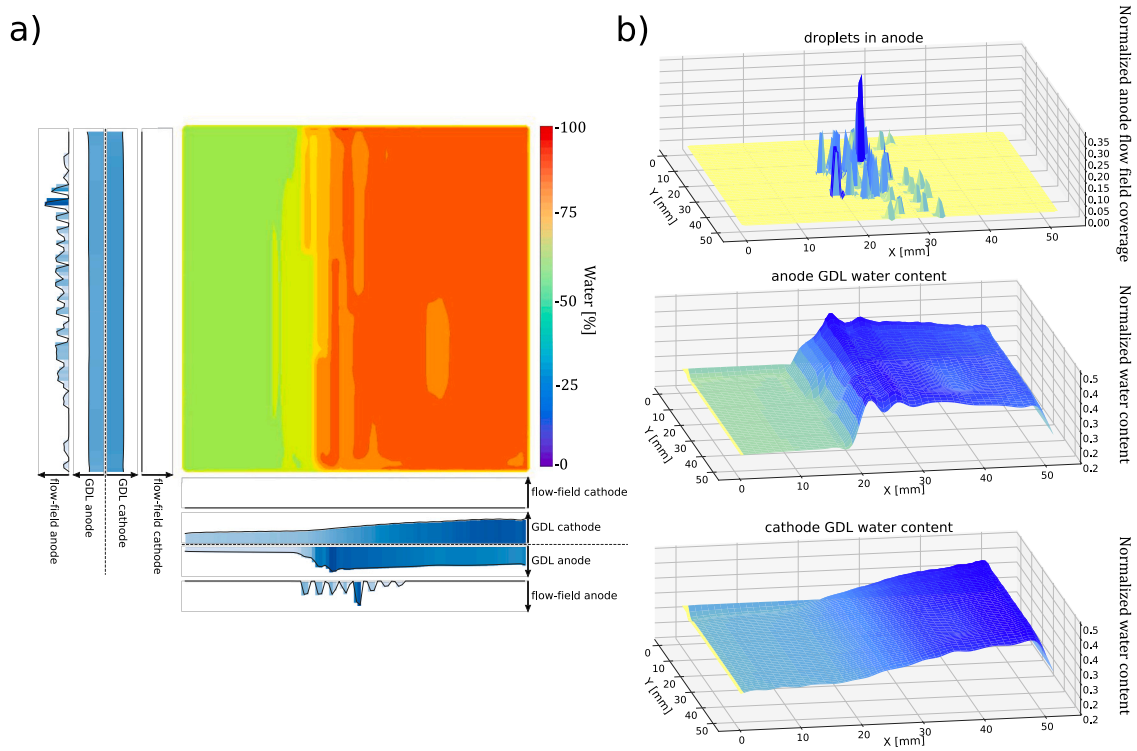
Fig. 4. Simulation results at experiment time 10 s (blue marker on Fig. 3) (a) Water content in the cell in the three spatial axes, (b) in-plane water content distribution in the anode flow field, and in the anode and cathode GDLs.
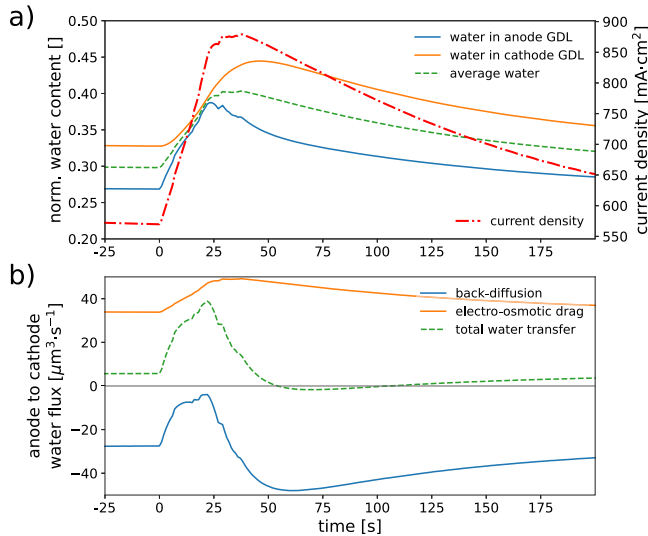

Fig. 5. (a) amount of water in each side of the cell and (b) water transfer contribution being the total water transfer the difference between back-diffusion and electro-osmotic drag.

400 measurement points, n_p.

$$\overline{x_t^h} = \frac{1}{n_p} \sum_{i=1}^{i=n_p} x_{t,i} \tag{2}$$

$$\sigma_{x_t}^h = \sqrt{\frac{1}{n_p - 1} \sum_{i=1}^{i=n_p} \left(x_{t,i} - \overline{x_t^h} \right)^2} \tag{3}$$

In this work, the values of variables below percentile 5% and over 95% have been discarded to avoid punctual effects altering the analysis,

Eq. (4).

$$x^* = \{ x_i, \forall x_i \in \left(p_{5\%}, p_{95\%} \right) \} \tag{4}$$

The average time value of variable x, $\overline{x^s}$, is the temporal average of spatial value $\overline{x_t^h}$ in experiment duration, T, as is shown in Eq. (5). The time standard deviation (SD) of a variable x, $\overline{x^s}$ is calculated using Eq. (6), which is an accurate indicator of the stability of a configuration.

$$\overline{x^s} = \frac{1}{T} \sum_{t=1}^{t=T} x_t^h \tag{5}$$

$$\sigma_x^s = \sqrt{\frac{1}{T-1} \sum_{t=1}^{t=T} \left(x_t^h - \overline{x^s} \right)^2} \tag{6}$$

The temporal and spatial analysis are summarized in Table (S1) (attached as supplementary data). The variables calculated in the temporal and spatial analyses are shown in Table 2.

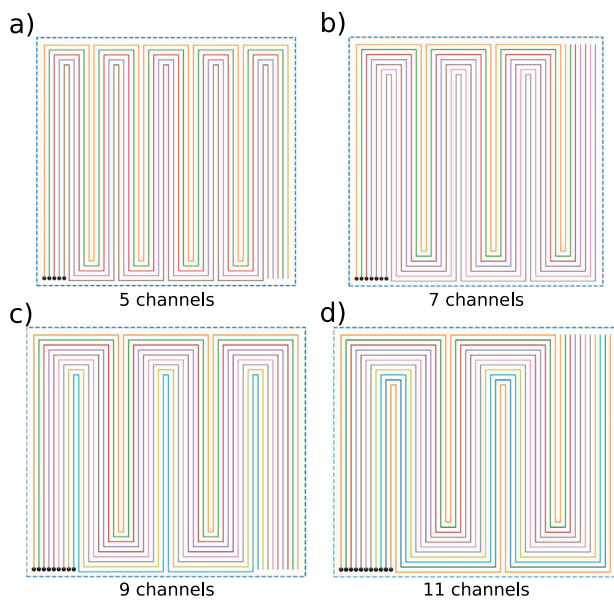### 5.1. Simulations of parallel serpentine channels

The single serpentine flow field design causes gas to flow at high speed because all the gas flows through a single long channel, which also causes a significant pressure drop. The multiple parallel serpentine designs reduce each channel's length, reducing the pressure gradient along each channel. However, lower speed in each channel may affect liquid water removal for the same overall flow rate.

In Fig. 6, the 4 serpentine designs used in this work are presented. This figure shows that the cell widths vary slightly to adjust to an integer number of channels and loops.

All parallel serpentine channel designs meet the condition that w_t, defined as the sum of the channel and rib widths (i.e., $w_c + w_r$), equals 2 mm. Cathode and anode counter flow setup is applied in this study. The effect of channel height is not studied, and it is not part of the experiment design of this work.

Table 2
Stability and homogeneity parameters.

Symbol	Definition	Dimension
$\overline{j}_t^h$	Average current density	Spatial
$\sigma_{j_t}^h$	Current density SD	Spatial
$R_{j_t}^h$	Current range	Spatial
$\overline{v}^s$	Average voltage	Temporal
σ_v^s	Voltage SD	Temporal
R_v^s	Voltage range	Temporal
$\overline{P}_t^s$	Average power density	Temporal
σ_P^s	Power density SD	Temporal
$\overline{r}_e^s$	Average evaporation rate	Temporal
$\sigma_{r_e}^s$	Evaporation rate SD	Temporal
$\overline{r}_w^s$	Average liquid water removal rate	Temporal
$\sigma_{r_w}^s$	Liquid water removal rate SD	Temporal
$\overline{W}^s$	Average normalized water content in cathode or anode	Temporal
σ_W^s	Normalized water content in cathode or anode SD	Temporal
$\overline{p}^s$	Average pressure drop	Temporal
σ_p^s	Pressure drop SD	Temporal
$\overline{u}_g^s$	Average gas speed	Temporal

Fig. 6. Representation of 4 parallel serpentine flow field designs used in the homogeneity study. From left to right, number of serpentine channels and MEA surface (a) 5 channels, 10 × 10.4 cm, (s.4, s.8, s.12, s.16, s.20, s.24, s.28, s.32, s.36) (b) 7 channels, 10 × 10.2 cm (s.3, s.7, s.11, s.15, s.19, s.23, s.27, s.31, s.35), (c) 9 channels, 10 × 11.2 cm (s.2, s.6, s.10, s.14, s.18, s.22, s.26, s.30, s.34), and (d) 11 channels, 10 × 11.4 cm (s.1, s.5, s.9, s.13, s.17, s.21, s.25, s.29, s.33).

The total number of experiments resulting from the combination of the model parameters is 36, which are numbered from s.1 to s.36, as are shown in Table 3.
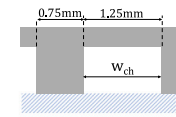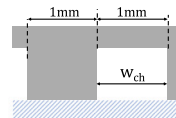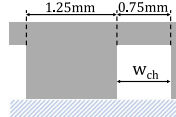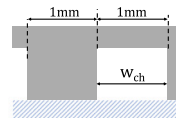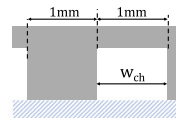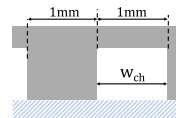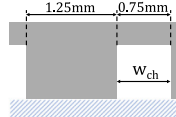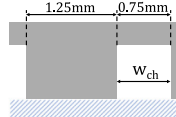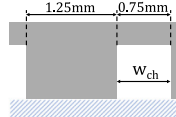
The complete temporal and spatial results of simulations are shown in Table S1 (attached as supplementary data).

Through temporal analysis, s.1, s.2, s.3, and s.5 simulations show flooded cells. Those simulations are setups with wider channels and lower stoichiometry ratios. The simulation becomes highly unstable computationally if the liquid water floods the channels and the gas flow cannot remove the water. The simulation s.6, while being stable, performs at levels far from the other simulations. Therefore, this simulation has been removed from the study as well.

The relationship of voltage SD, σ_v^s, with the cathode gas speed, $\overline{u}_{c,g}^s$, shows that the stability is increased when the gas flow increases (in Fig. 7a the crosses and arrows represent values out of range or unstable simulations). Low gas speed in the channel reduces the capability of removing water droplets from the channel [10]. A higher number of

Table 3
Design table of simulated experiment varying parameters: channel–rib width ratio, w_c/w_r, number of channels in the flow field, # channels, and stoichiometry ratio, R_{st}.

ID #	w_c/w_r	# channels	R_{st}
s.1-s.4	5/3	11,9,7,5	1.0
s.5-s.8	5/3	11,9,7,5	1.3
s.9-s.12	5/3	11,9,7,5	1.7
s.13-s.16	1	11,9,7,5	1.0
s.17-s.20	1	11,9,7,5	1.3
s.21-s.24	1	11,9,7,5	1.7
s.25-s.28	3/5	11,9,7,5	1.0
s.29-s.32	3/5	11,9,7,5	1.3
s.33-s.36	3/5	11,9,7,5	1.7

channels and a smaller stoichiometric ratio cause a low gas speed through the channels. The gas speed has been used as a parameter that combines those two parameters, the stoichiometric ratio and the channel width.

Fig. 7b shows the evolution of spatial current density SD with respect the gas speed. From the data is observed that an increase in gas speed produces an increase in spatial current density SD, σ_j^h.

The dependence of voltage SD on channel number and channel–rib ratio (ratio C–R) is illustrated in Fig. 8. This figure shows that a higher stoichiometry ratio makes the simulation more stable in time. Moreover, it can also be observed that, especially on low stoichiometry ratios, lower C–R ratios and lesser numbers of channels provide more stable solutions.

Fig. 9 shows the values of current density homogeneity, $\sigma_{j_t}^h$, by ratio C–R and number of channels grouped by stoichiometry ratio. The gray bars represent the unstable simulations; therefore, the result is not valid for analysis. The results show the importance of narrower channels, in which the 3/5 C–R ratio performs better in spatial homogeneity than the 5/3 and 1 values.

Time evolution of RH, gas pressure drop inlet–outlet, and presence of liquid droplets in the flow field influence spatial homogeneity. Therefore, higher flows increase the homogeneity, $\sigma_{j_t}^h$. However, the spatial homogeneity does not always improve when increasing the stoichiometry ratio for the lower number of channels or ratio C–R, as is shown in Fig. 9. Nevertheless, the increasing stoichiometry ratio improves the cell's performance uniformity, especially for higher C–R ratios and the number of channels. A uniform setup with low stoichiometry ratios is more efficient in fuel consumption. In the range of configurations simulated, the setup that uses 7 channels performs better than the rest in terms of spatial and temporal uniformity, especially when low stoichiometry ratios are used.

As an example, two different simulations are compared in Fig. 10: (a) simulation s.11 with 7 channels, C–R ratio 5/3 and stoichiometry ratio 1.7; and (b) simulation s.35, with the same experimental setup but using C–R ratio 3/5. In the figure, the differences in spatial homogeneity are observed.

From the simulations, in terms of outlet pressure in the cathode or the anode, no distinctive trends are observed in absolute terms in temporal analysis, but the outlet pressure SD is reduced as the flow increases, similarly to voltage SD. The spatial analysis has not been performed since only a point is evaluated for each outlet pressure.
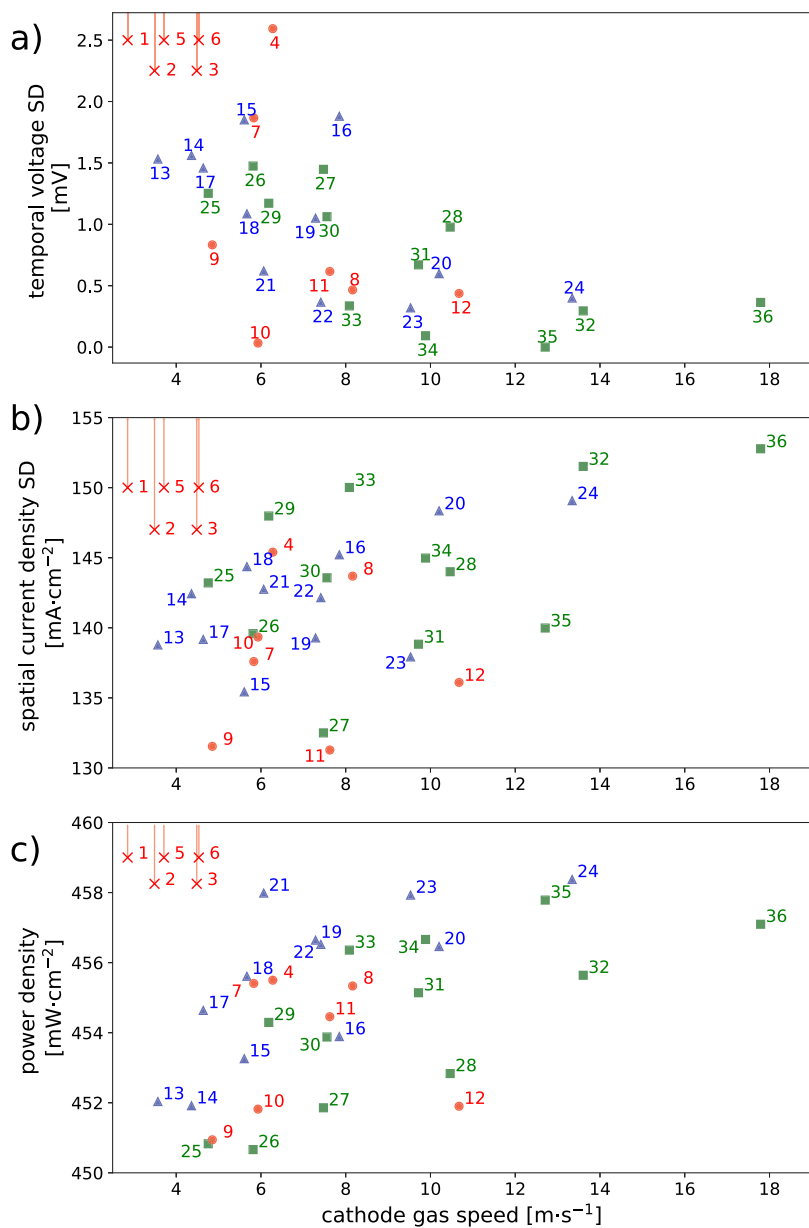
Fig. 7. Relationship of (a) voltage SD, σ_v^s, (b) spatial current density SD, $\sigma_{j_i}^h$, and (c) average power density, $\overline{P}_t^s$, of the different simulation setups with the nominal gas speed of the cathode.
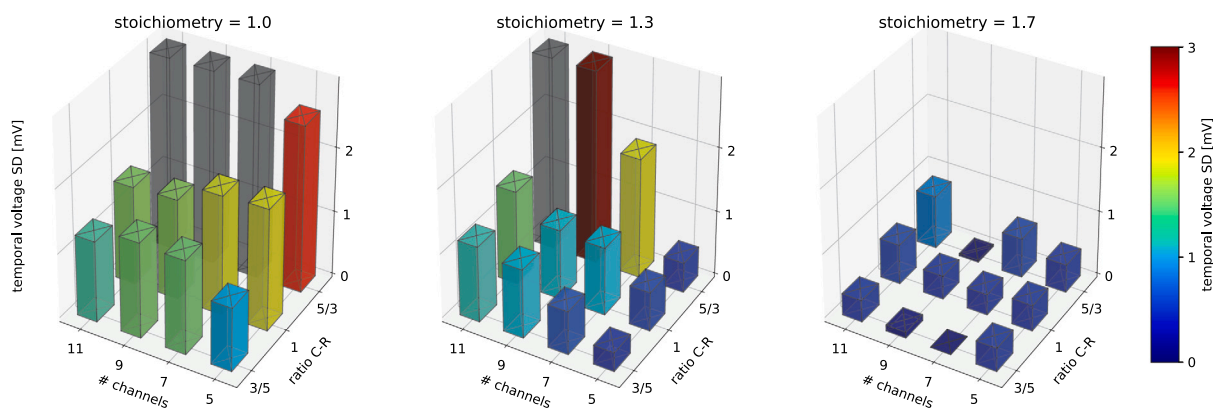

Fig. 8. Voltage SD related to the number of channels, ratio C–R and stoichiometry ratio.
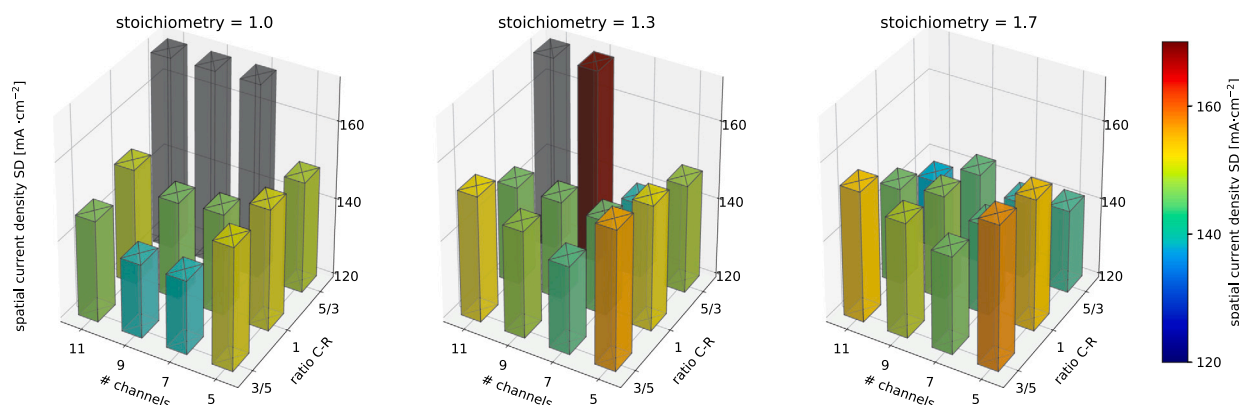
Fig. 9. Spatial current density SD at the time 500 s related to the number of channels, the C–R ratio, and the stoichiometry ratio.
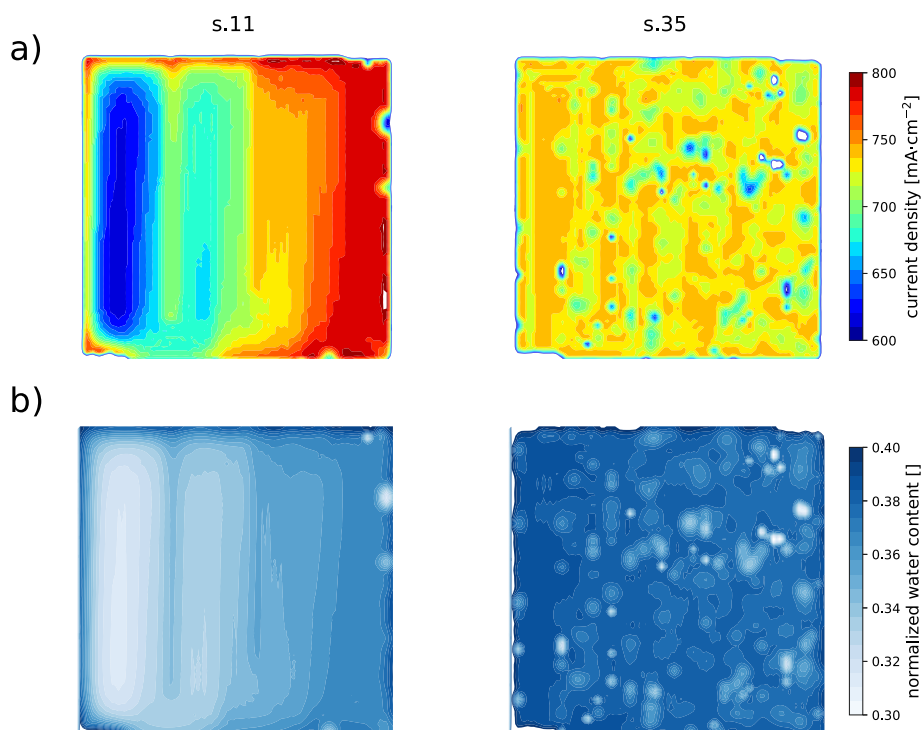

Fig. 10. Spatial current density and water content comparison between simulation s.11 and s.35 at the time step 500 s. Seven parallel serpentine channels and 1.7 cathode stoichiometry are used in both configurations. The C–R width ratio is 5/3 for s.11 and 3/5 for s.35.

5.2. Simulations of parallel channels

Parallel straight channels are analyzed in this section to compare with parallel serpentine channel configurations. The parallel straight channels have been designed with 10×10 cm area and 0.75 mm channel width. This configuration has 48 parallel channels. The effect in performance uniformity for 4 different gas flow values has been analyzed.

It is observed that there is an agreement between the simulation results obtained from the parallel and the serpentine parallel channels configuration. The effect of gas speed inside the channel is a critical factor in the uniformity of the cell. Higher stoichiometric ratios for parallel channels are required, compared to parallel serpentine channel designs, to remove the liquid water. With the experimental configuration employed in this paper, the efficiency of the system is reduced, as it would require fuel recovery to make the solution economically feasible.

The current density pattern and the water content distribution in the cell of the parallel straight channel configuration can be observed

in Fig. 11. From the figure it can be observed the up-to-bottom pattern due to the orientation of the channels.

6. Simulation performance

To evaluate the simulation performance of the model, three different cell designs, using different MEA sizes, have been chosen (141 cm^2, 100 cm^2, and 25 cm^2): (a) a 141 cm^2 cell with 23 channels of a 0.8×0.8 mm^2 cross-sectional area (0.7 A·cm^{-2} galvanostatic mode, 1.5 atm of inlet pressure fed with air and pure hydrogen operating at 80 °C. Nafion XL as a membrane and Sigracet 25 BC as GDLs); (b) 100 cm^2 cell with 11 channels of 1×1 mm cross-sectional area with constant RH (used in parameter studies); and (c) a 25 cm^2 cell with 1×1 mm single serpentine cell operating at steady state and in drying–humidifying cycles respectively (used on the model validation).

Although the setup conditions applied for each of the studied active areas are different, the results are presented to estimate the ranges of simulation times in each one of the submodels.
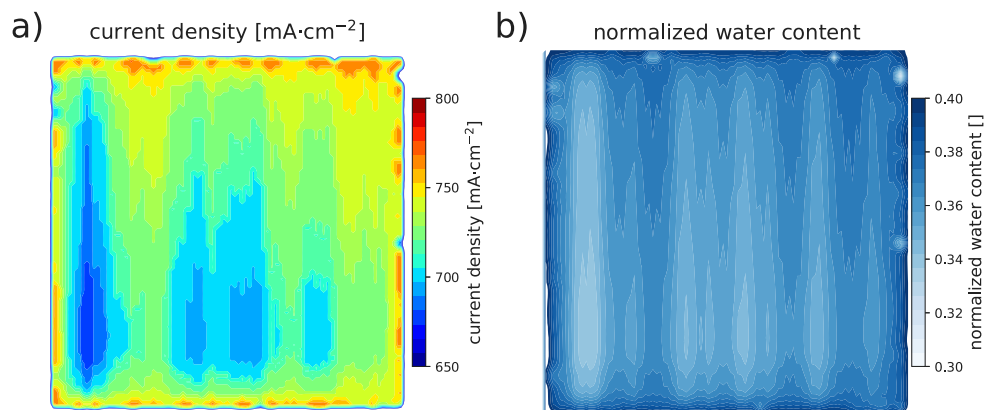
Fig. 11. Parallel straight channel with stoichiometry ratio 5 (a) spatial current density map and (b) water content distribution.

Table 4
Computation time to simulate of one time step (1 s) for 25 cm², 100 cm² and 141 cm² cell surface.

Subprocess Id.	25 cm² [s]	100 cm² [s]	141 cm² [s]
Update parameters	0.04	0.06	0.06
Channel solver	0.98	7.53	14.19
Water balance	0.26	2.28	4.12
GDL gas diffusion	0.05	0.7	0.6
GDL water diffusion	0.35	0.5	0.5
Electro-chemical reactions	0.05	1.4	1.8
Membrane water balance	0.5	2.4	5.9
Save data	1.93	8.7	8.2
Total	4.16	23.57	35.37

For the 25 cm², 100 cm² and 141 cm² cell sizes, 1 s simulated time, on average, required 4.16 s, 23.57 s, and 35.37 s the CPU time, respectively. For simulation time of 100 s, spent 7 min (410 s), 39 min (2357 s), and 58 min (3490 s). And for 1000 s of simulation time, spent 68 min (4100 s), 392 min (23570 s), and 581 min (34900 s).

Table 4 shows the computational cost of each part of the simulation procedure for 1 s of simulation time and the different cell sizes. These times are not constant and may fluctuate slightly during the simulations. Table 4 shows that the channel submodel simulation is the most computationally expensive process because it represents the movement of water droplets in the channels. Both the channel, the gas and water diffusion in the GDLs, and the water balance in the MEA submodels have been implemented in the C++ language.

In Table 4 is observed that some time procedures are similar independently of the dimension of the cell.

The simulation time of the electrochemical reaction, the GDL species diffusion, the water balance, and the membrane balance submodels depend linearly on the number of elements.

The model simulations have been executed in a 6 core Intel Xeon processor E5-2620 v3, 64 Gb of RAM, using SSD hard disk and windows 10 operating system. Python and C++ routines were executed in single-core mode. The simulation of the 141 cm² cell used up to 500 MB of RAM memory. The simulating results show excellent performance in terms of computational effort compared with much more complex models [32], which take days to complete the simulation. Similar studies have required high-capacity computing equipment to perform the simulations, such as in [53], whose simulations were conducted on a super-computing cluster optimized for fluid dynamics.

7. Conclusions

This paper shows the development of a pseudo-3D dynamic model of PEFC. This model is able to represent the water management of the liquid and gas phases at the anode and cathode, including the movement of liquid water in the channels. In addition, the simulation procedure allows for studying different flow field designs. The simulation procedure and the model have been developed to optimize the computational effort, allowing long-term simulations in a short time without compromising the accuracy of results. For this purpose, a sequential solving methodology, dimensional reduction of models, and the implementation of the most computationally intensive simulation procedures in C++ have been used. This optimization allows solving, for example, 100 cm² cells with 11 parallel channels with less than 25 s per second simulated.

The model has been validated with a 25 cm² single serpentine cell exhibiting dynamic behavior of re-humidification via water droplets.

In this work, a study of spatial homogeneity and temporal stability has been carried out, considering that it is a key factor in the cell's durability. The effect of different flow field configurations, the number of parallel serpentine channels, the ratio between channel and rib width, and stoichiometry on long-term spatial and temporal uniformity have also been evaluated.

Some conclusions from the simulations obtained are shown below:

- Based on the results with 50% RH of gases in the flow field feeding, the gas flow must be sufficiently high to remove the liquid water droplets by dragging them out of the channels.
- According to the experiments shown in Section 4.1, and a consequence of the previous point, the number of channels and the stoichiometry must ensure a sufficient gas flow in the channel for the liquid water removal.
- Under the conditions studied, higher gas flows decreases the temporal voltage SD as the residence time of a droplet inside the flow field decrease as gas flows increase.

Within the studied range of configurations in steady state at 50% RH of gases in the anode and cathode feeding, the better performing configuration in terms of stability and uniformity is one of 7 channels with the narrower channels (0.75 mm width). This configuration provides a high gas flow per channel at a low stoichiometry ratio, enabling the removal of the liquid water droplets. Moreover, the number of turns is lower than in a 5-channel configuration, reducing the spatial non-uniformity and the pressure losses due to the effect of the corner. In the case of the cell configurations simulated, the optimum design was obtained using between 5 and 7 parallel serpentine channels, a channel/rib ratio of 3/5, and stoichiometric ratios of 1.3 and 1.7. These differences can be observed comparing simulated case test 14 (channel/rib ratio = 1, stoichiometry = 1, channels = 9) with test 31 (channel/rib ratio = 3/5, stoichiometry = 1.3, channels = 5), where the power density and the spatial current density SD slightly vary (0.7% and 2.8%) but the temporal stability decreases up to 58% from test 14 to test 31.

In future work, other parameters that significantly affect the uniformity of operation will be studied, such as the total current density and the dynamic and spatial effect of temperature, which have an important impact on the water management in the cell. The dynamic cell degradation phenomena will also be considered in the future development of the model. These new features, incorporated in the model, would be applied to evaluate non-stationary operation profiles using the capability of long-term simulation methodology.

CRediT authorship contribution statement

S. Culubret: Software, Resources, Project administration, Methodology, Investigation, Funding acquisition, Formal analysis, Data curation, Conceptualization, Supervision, Validation, Visualization, Writing – original draft, Writing – review & editing. **M.A. Rubio:** Writing – review & editing, Writing – original draft, Visualization, Conceptualization, Data curation, Formal analysis, Funding acquisition, Investigation, Methodology, Project administration, Resources, Software, Supervision, Validation. **D.G. Sanchez:** Writing – review & editing, Writing – original draft, Supervision, Resources, Methodology, Investigation, Formal analysis, Conceptualization. **A. Urquia:** Writing – review & editing, Writing – original draft, Supervision, Project administration, Methodology, Investigation, Funding acquisition.

Declaration of competing interest

The authors declare that they have no known competing financial interests or personal relationships that could have appeared to influence the work reported in this paper.

Data availability

Data will be made available on request.

Acknowledgments

Appendix A. Model development

This model combines sub-models with different dimensionality, which are connected to allow a complete dynamic representation of the cell. The sub-models represent each component of the cell:

- GDL model represents the gas and water diffusion in the plane XY (2D model). Liquid water removal due to capillary pressure is evaluated in the perpendicular plane axis, Z (1D model).
- Membrane layer model. The water transport due to electro-osmotic drag and back diffusion is represented by this sub-model (0D model).
- Flow field model describes (a pseudo-3D model based on a 1D model) the gas transport and pressure losses, and the water droplets' movement.
- Electrochemical model (0D model). This model allows calculating the current, voltage, and fuel gas balances in function of the concentrations and pressures of gases.
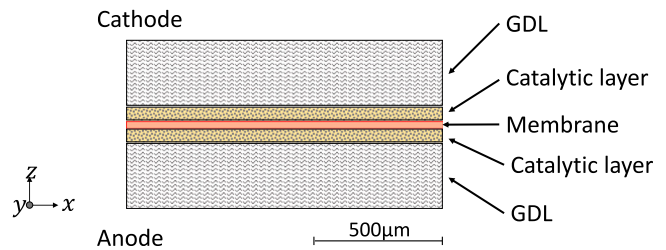

Fig. A.12. MEA components.

The pseudo-3D fuel cell model has been designed to simulate transient and spatial behaviors with low computational cost. The model has considered two main physical components: the MEA and the flow fields. The MEA is composed of 5 elements, as shown in Fig. A.12.

This diagram shows the cathode and anode GDLs, which typically have a thickness of around 200 μm. The catalytic layers are where the electrochemical reactions occur, and their thickness is typically 5 μm. Finally, the membrane component is the one that enables proton conductance while acting as a reactant barrier and electronic insulator to avoid short circuits between the anode and cathode. Typically has a thickness of 25–30 μm. The cell geometries analyzed in this paper are 5×5 cm^2 and 10×10 cm^2. In those cells, the XY dimensions are around 10^2 times more significant than the Z dimension.

Our approach in developing the model has been to reduce the computational effort, mainly considering the plane XY where most of the non-uniformity occurs; simplifying the flow field model into 1D linear models; considering the behavior of liquid droplets as constant volume elements which may clutter along the path but not break among others. Also, the channels are considered linear elements where gases and droplets move along, exchanging water with the GDL. The serpentine shape studied in this paper can be up to 50 cm in length and 0.1×0.1 cm^2 channel cross-section. Therefore, the effect on channel length is more relevant than its cross-section in terms of variability.

A.1. Gas diffusion layer model

The GDL is responsible for: (a) allowing gases diffusion; (b) removing water from the catalytic layers; (c) the support of the membrane; and (d) the electric conduction. Due to the first two properties, GDL must be a porous media that allows gases to flow through it. In addition, it is usually treated with highly hydrophobic materials to ensure proper water removal [56]. Ideally, the width of GDL may be reduced, but because the membrane is thin (about 25 μm [54]) requires some support material. In its absence, the membrane could easily break.

The liquid water in the GDL clogs some pores impeding the gas from crossing through them. In the model presented in [32], a combination of the flow field and GDL models was developed using commercial software (ANSYS). However, since the diffusion time constants of gas and water are significantly different (gas diffusion is between 10^{-3}–1 and water diffusion around 1–10^3 s) [25], both phenomena can be calculated independently in the model, allowing the decoupling of phenomena [57].

A.1.1. Gases diffusion within the GDL

The gases used in fuel cells are usually a mix of species. The anode is fed with high purity hydrogen and steam water, and the cathode is typically fed with air (O_2, N_2 and H_2O). Therefore, multi-component Stefan–Maxwell equations are suitable to represent the gases diffusion Eqs. (A.1), (A.2).

$$\sum_j A_{i,j} J_i = \nabla \left(\frac{C_i}{|C|} \right) \tag{A.1}$$

$$A_{i,j}(C) = \frac{C_i}{\|C\|^2}\begin{cases}\sum_{l\neq i}\frac{-C_l}{D_{i,l}} & \text{if } i = j \\ \frac{C_i}{D_{i,j}} & \text{if } i \neq j\end{cases} \tag{A.2}$$

Eq. (A.1) is a tensor equation relating the molar fluxes, J_i, with the concentration of each species, C_i. The matrix $A_{i,j}$ defines the fluxes relationship with the concentration in each coordinate axis. The parameter $D_{i,j}$ is the binary diffusion between species.

In equation Eq. (A.2) $\|C\|$ represents the sum of the concentrations and $|C|$ in Eq. (A.1) represents the norm of the concentrations vector.

A simplification of Stefan–Maxwell's equations is described by [35] where a multi-component Fickian diffusion is used, reducing the numerical computations. This approach allows calculating the pressure gradient along the GDL using Fick's diffusion second law Eq. (A.3) [58].

$$\frac{\partial P}{\partial t} = D_{i,j}\frac{\partial^2 P}{\partial x^2} \tag{A.3}$$

Although the computational effort is reduced using the multi-component Fickian diffusion, a single gas formulation is used to reduce the number of calculations further.

This simplification uses the combined gas-mixture properties to represent a single gas instead of a multi-component approach.

The gas diffusion coefficient depends on GDL's porous material properties, such as porosity, ϵ, tortuosity, τ, and the liquid content, s. The amount of water becomes relevant as reduces the number of pores of the material Eqs. (A.4), (A.5) [59].

$$\epsilon_0 = \frac{V_{pore}}{V_{total}} = \frac{V_{pore,0} - (V_{total} - V_{pore,0})\,s}{V_{total}} \tag{A.4}$$

$$D_{eff} = D\epsilon^\tau \tag{A.5}$$

A.1.2. Water transport within the GDL

The water flow in porous media is described by Eq. (A.6). The water flow due to capillarity on GDL was studied in [60,61].

$$\frac{dp}{dt} = \frac{\kappa}{\epsilon\mu c_t}\frac{d^2 p}{dx^2} \tag{A.6}$$

Where ϵ is the material's porosity, μ is the dynamic gas viscosity, κ is the permeability, and c_t is the combined compressibility of gas and the porous media. Leverett's equation defines the capillary pressure, p_{cap}, on the GDL. The Eq. (A.8) represents the capillary pressure as a function of the actual volume fraction of liquid, s, inside a porous media (for contact angles over 90 degrees) and the material properties described in [57]. The capillary pressure depends on the material's contact angle, θ_s, permeability, and porosity. Leverett's equation is a function of the water content in the porous media, s.

$$p_{cap} = \frac{\epsilon\sigma\cos\theta_s}{\kappa}J(s) \tag{A.7}$$

$$J(s) = 1.417s - 2.120s^2 + 1.263s^3 \tag{A.8}$$

A.1.3. Liquid water removal from the GDL

The liquid water in GDL is expelled as a consequence of overcoming the capillary pressure limit defined by Young–Laplace Eq. (A.10), and the actual capillary pressure in the GDL Eq. (A.9) [62,63]. This equation defines the drainage produced when the liquid pressure, p_{liq}, minus the pressure of the gas, p_g, is higher than the capillary pressure, p_{cap}, which depends on the porosity and the surface tension of the liquid.

$$p_{cap} = \frac{2\gamma\cos(\theta)}{R_{pore}} \tag{A.9}$$

$$p_{liq} - p_g > p_{cap} \tag{A.10}$$

The uptake of liquid water from a porous material depends on the water liquid content, s, the gas pressure, p_{gas}, the capillary pressure of porous media, p_{cap} and the average pore radius, R_{pore}. The
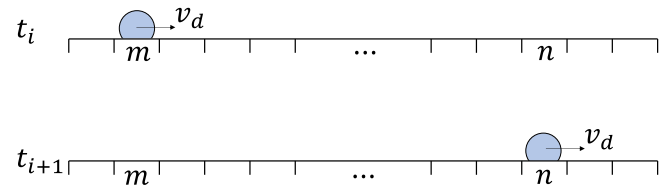

Fig. A.13. Droplet movement in a 1D channel during a time interval.

liquid water is drained from the porous media if the condition of Eq. (A.10) is satisfied. As the GDL is typically treated with hydrophobic chemicals [62,63], the capillary pressure value is negative. The liquid expelled from the GDL becomes water droplets on its surface. The liquid water flows expelled through the capillary is defined by Eq. (A.11), which depends on the permeability, κ, and dynamic viscosity, μ.

$$\dot{w} = \frac{\kappa A}{\mu}\frac{dp}{dx} \tag{A.11}$$

A.1.4. Liquid water re-absorption into the GDL

The re-absorption model can be mathematically described as shown in Eq. (A.12).

$$\dot{w}_a = \delta_{V,drop}\left(D_{ra}\left(s_{min} - s_{r,i}\right)\right) \tag{A.12}$$

Where $\dot{w}_a$ represents the water flow during the re-absorption, $\delta_{V,drop}$ represents the minimum droplet size the enable re-absorption, D_{ra}, represents the re-absorption capabilities of the surface, and $s_{r,i}$ the amount of water on the element where the droplet is standing at the time of the calculation. The simulation of the equations representing these phenomena in a discrete-time model is computationally expensive, since the time steps must be sufficiently small to match the droplet movement and continuous humidification. An average trajectory strategy is proposed to reduce the computational effort. A droplet, d, in the channel, represented in Fig. A.13, during the time interval t_i to t_{i+1} has advanced from x_i to x_{i+1}. The trajectory of the droplet passes over the regions of the channel path from x_m to x_n, where each region has different water contents (w_h). The proposed method consists of calculating the average water in all regions from x_m to x_n, $\overline{w}_{m\rightarrow n}$ and distribute it accordingly to the amount of water in each region.

$$w_a = \delta_{V,drop}\left(D_{ra}\delta_{w_i - w_{min}}\left(w_{min} - \overline{w}\right)\right)dt \tag{A.13}$$

$$w_{a,h} = \frac{w_h}{\sum_m^n w_k}w_a \tag{A.14}$$

A.1.5. Water evaporation and condensation from the GDL

The water evaporation and condensation from the channel is represented by Eq. (A.15). The condensation of water from the GDL is obtained using Eq. (A.16) [53,64].

$$S_{vl,evp} = k_{evp}\epsilon s\frac{\rho_{liq}}{M_{H_2O}}\left(p_{H_2O} - p_{H_2O}^{sat}\right) \tag{A.15}$$

$$S_{vl,con} = k_{con}\epsilon(1 - s)\frac{X_{H_2O}}{RT}\left(p_{H_2O} - p_{H_2O}^{sat}\right) \tag{A.16}$$

The water evaporation rate, $S_{vl,evp}$, depends on the relative humidity of the gas represented by steam water pressure, p_{H_2O}, and the liquid water content in the GDL, s.

A.2. Membrane model

The membrane is a reactants barrier while acting as a proton conductor. Proper membrane hydration is essential for cell performance since it affects the polymer electrolyte conductivity. Water is also capable of crossing the membrane. Two mechanisms drive the water crossing the membrane. The electro-osmotic drag is the water flow

dragged due to protonic local current density, Eq. (A.17). The back-diffusion is the water flow due to the difference of water concentration on both sides of the GDL, Eq. (A.19) [52].

$$J_{eo} = 2n_d \frac{j}{2F} \tag{A.17}$$

$$n_d = 0.0029\lambda_m^2 + 0.05\lambda_m - 3.4 \cdot 10^{-19} \tag{A.18}$$

$$J_{bd} = -D_{bd} \frac{d\lambda_m}{dz} \tag{A.19}$$

Where n_d is the electro-osmotic drag coefficient which depends on the degree of humidification of the membrane (λ_m), the current density, j, and the Faraday constant, F.

A.3. Flow field model

The flow field model is a superposition of 1D models allowing to represent 3 dimensions (pseudo-3D). This model considers the effect of pressure losses due to: (a) gas and liquid flow; (b) channel geometry; (c) resistance to gas flow caused by the water droplets in the channels; and (d) consumption of reactive gases due to gas consumption.

The pressure losses due to the flow of gases and liquid water in a channel are represented by Darcy–Weisbach's Eq. (A.20). This equation describes the pressure losses for a specific fluid at a certain speed, u, through a tube of known hydraulic diameter, D_h, and length, L. The density of the air is calculated as a mix of the dry air density and water content per free flow volume.

$$\frac{\Delta p}{L} = f \frac{\rho u^2}{2D_h} \tag{A.20}$$

The Darcy friction coefficient, f, is calculated in the laminar regime and turbulent flow using the Colebrook–White, Eq. (A.21).

$$f = \begin{cases} \frac{64}{Re} & \text{if } Re < 2300 \\ \left(-\log\left(\frac{e_r}{3.7 D_h} + \frac{2.51}{Re\sqrt{f}} \right) \right)^{-1} & \text{if } Re \geq 2300 \end{cases} \tag{A.21}$$

Darcy–Weisbach's equation is used to represent other channel geometries since the *equivalent length method* can be applied in the turns of the channels.

The equivalent length method is used to describe the pressure loss through an elbow of the channel as a length of straight channel. Data tables [65] have been employed, which allow to calculate the equivalent length L_e function of the channel hydraulic radius.

A.4. Droplet dynamics

The droplet dynamics were analyzed in [42,43,50,51]. In these flow field geometric models, the deformation of the droplet is taken into account to calculate the adhesion and dragging force under the action of a gas flow. This process requires considerable computational effort to calculate the current deformation state due to the droplet's advance. Those models are widely used to calculate droplet detachment or oscillation frequencies of a droplet under specific flow values in the channel. In the developed model, an approximation of the displacement of a droplet in a non-linear channel is required. The water droplet model works successfully on straight channels with a single contact surface. The model has to be extended to consider channel turns and the contact of droplets with multiple walls.

Three angles define the geometrical droplet deformation: the advancing angle, θ_a, the receding angle, θ_r, and the static contact angle with the surface, θ_s. The droplet deformation is illustrated in Fig. A.14.

The droplet radius, R_d, chord length, c_d, Eq. (A.24), the area, A_d, Eq. (A.26), and the height, h_d, Eq. (A.28) are calculated considering the angles and the droplet volume. The geometrical description of droplet allows the calculation of the different forces in the geometrical model.

The chord is considered to be constant, relating static contact angle θ_S, advancing angle θ_A, and receding angle θ_R. The droplet area and the droplet height, static and dynamic, enable the calculation of gas drag force, as is the area upon which it acts, and the Reynolds number, respectively.

$$V_d = \frac{\pi D_d^3}{24} \frac{2 - 3\cos\theta_s + \cos^3\theta_s}{\sin^3\theta_s} \tag{A.22}$$

$$c_s = 2\sin(\theta_s) R_s \tag{A.23}$$

$$c_d = \frac{R_d}{\sin\theta_s} \left(1 + \sin\theta_A \sin\theta_R - \cos\theta_A \cos\theta_R \right) \tag{A.24}$$

$$A_1 = \theta_A + \theta_R - \sin(2\theta_A) + \sin(\theta_A - \theta_R) \tag{A.25}$$

$$A_d = \frac{R^2}{2\sin\theta_R} \left(A_1 \sin\theta_R + \sin^3 \frac{\theta_A - \theta_R}{2} \sin \frac{\theta_A + \theta_R}{2} \right) \tag{A.26}$$

$$A_s = R_s^2 \left(\theta_s - \frac{\sin(2\theta_s)}{2} \right) \tag{A.27}$$

$$h_d = R_d \left(1 - \cos\theta_A \right) \tag{A.28}$$

As the chord remains constant along the droplet deformation, it is possible to find a relationship between receding and advancing angles for a given droplet volume.

The adhesion force is calculated integrating the surface tension of the droplet, γ, over the length of the droplet contact line Eq. (A.30). The dragging force depends on the gas flow and the sectional area of the channel, Eq. (A.29).

$$F_{drag} = \frac{1}{2} \rho_{gas} u_{gas} C_d A_d \tag{A.29}$$

$$F_{adh} = -\gamma \int_0^l \cos\theta(l) \cos\psi(l) \, dl \tag{A.30}$$

In Eqs. (A.29), (A.30), θ represents the contact angles. The adhesion force integral can be simplified into Eq. (A.31).

$$F_{adh} = k_{adh}\gamma w_d \left(\cos\theta_R - \cos\theta_A \right) \tag{A.31}$$

The constant k_{adh} depends on the droplet shape. The value of k_{adh} varies between $\frac{\pi}{2}$ and $\frac{\pi}{4}$ depending on the values obtained analytically or through the finite element [50]. The droplet width is represented by w_d, where R_d, and γ represent the radius and the tension surface of a spherical liquid droplet, respectively. The droplet dynamics are fully described using Eqs. (A.29), (A.31), (A.34).

The droplet dynamics depend on the dragging force, F_{drag}, Eq. (A.32), which makes the droplet advance, and the adhesion force, F_{adh}, Eq. (A.35), where t_d is the contact line of the droplet. The Eq. (A.33) represents the resistance to the advance of the droplet. Therefore by using these forces differences and Newton's law, the movement of a droplet is described by Eq. (A.34).

$$F_{drag} = 0.5 \cdot C_d A_{c,drop} \rho_{gas} v_{gas}^2 \tag{A.32}$$

$$t_{d,s} = R_d \frac{\frac{4}{3}\pi - \frac{\pi}{3} \left(1 + \cos\theta_s \right)^2 \left(2 - \cos\theta_s \right)}{\theta_s - \frac{\sin(2\theta_s)}{2}} \tag{A.33}$$

$$m_d \ddot{x}_d = \delta_{drag>adh} \left(F_{drag} - F_{adh} \right) \tag{A.34}$$

With the aim of improving the simulation time, a model simplification has been applied. In solving the geometric model iteratively at each simulation step to compute the adhesion force, an approximation of the geometrical force function of the gas speed and the droplet speed has been used, Eq. (A.36). Therefore, in order to improve computational efficiency, $\Delta\theta$ is calculated from Eq. (A.36).

$$F_{adh} = 2\gamma t_d \Delta\theta \tag{A.35}$$

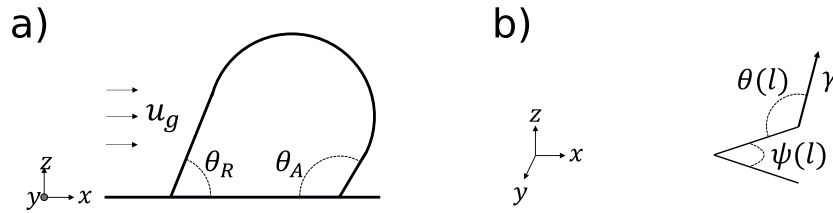$$\Delta\theta = K_{v,gas} v_{gas} + K_{v,drop} v_{drop} \tag{A.36}$$

Fig. A.14. (a) Deformed droplet due to air flow inside a channel and (b) contact line of the droplet with the surface.

A.5. Electrochemical model

As described by Eq. (A.37), the cell voltage depends on: (a) the reversible voltage (E_{oc}) defined by Gibbs; (b) the concentration overvoltage (V_{con}); (c) the activation overvoltage (V_{act}); and (d) the ohmic overvoltage (V_{ohm}).

$$V = E - V_{con} - V_{ohm} - V_{act} \tag{A.37}$$

$$E = E_{oc} + \frac{RT}{2F}\left(\ln\left(p_{H_2}\right) + \frac{1}{2}\ln\left(p_{O_2}\right)\right) \tag{A.38}$$

The cell potential is defined by the reactants pressures, p_{O_2} and p_{H_2}, and depends on the temperature, T.

The concentration overvoltage is related to the limitation on performance due to the lack of reactants supply. It is expressed as a function of the current density Eq. (A.39). In this paper, an extended version of [66] is used to represent the concentration of the reactants at each point of the cell Eq. (A.40). Where C_X and $C_{X,0}$ are the concentration and the minimum required concentration of H_2 and O_2.

$$V_{con} = 3 \cdot 10^{-5} e^{-8j} \tag{A.39}$$

$$V_{con} = \frac{RT}{\alpha n F}\ln\left(\frac{C_{O_2,i}}{C_{O_2,0}}\right) \tag{A.40}$$

The activation overvoltage is function of the current density at each point Eq. (A.41).

$$V_{act} = \frac{RT}{2F}\ln\left(\frac{j}{j_0}\right) \tag{A.41}$$

The ohmic overvoltage is an important part of the cell performance. It defines the linear component of the polarization curve in the typical operating range. The main component of the ohmic resistance, Eq. (A.42), depends on the membrane resistance, Eq. (A.43) and then on its water content, Eq. (A.44) at each point of the cell.

$$V_{ohm} = \frac{th_m}{\sigma_m} j \tag{A.42}$$

$$\sigma_m = \left(b_1 - \lambda_m b_2\right) e^{b_3\left(\frac{1}{300} - \frac{1}{T}\right)} \tag{A.43}$$

$$\lambda_m = \frac{WU}{IEC \cdot M_{H_2O}} \tag{A.44}$$

Where th_m represents the thickness of the membrane and σ_m is the conductivity of a fixed spatial point for a specific membrane state. Correctly calculating the conductivity is crucial for evaluating the performance of the cell. The Eq. (A.43) is used to calculate the membrane conductivity.

The variable λ_m depends on the water activity or alternative as shown in Eq. (A.44) on water uptake (WU), ion exchange capacity (IEC), and the molar mass of water. In other investigations [38], an alternate conductivity model was proposed.

$$\sigma_m = \begin{cases} 0 & \text{, if } W_U < W_{U_c} \\ \sigma_0\left(W_U - W_{U_c}\right)^{\beta} & \text{, if } W_U \geq W_{U_c} \end{cases} \tag{A.45}$$
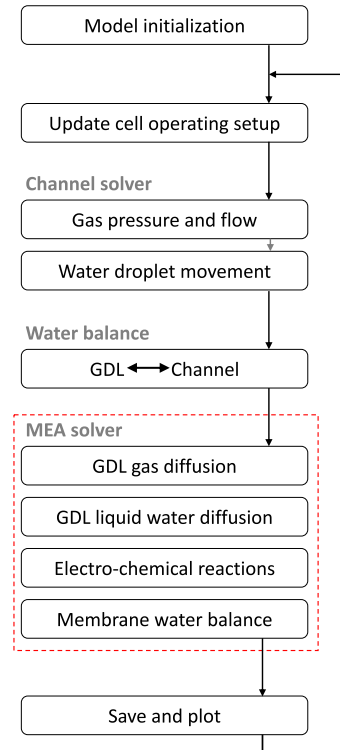

Fig. B.15. Scheme of simulation procedure. The red-dotted rectangle part of the solver is compiled in C++, the rest is implemented in Python.

Where WU is the rate between dry and wet membrane weight, which depends on the water content on the membrane and its initial weight, and is calculated by Eq. (A.46).

$$WU = \frac{m_{wet} - m_{dry}}{m_{dry}} = \frac{\left(m_{dry} + s\epsilon\rho_w V_m\right) - m_{dry}}{m_{dry}} = \frac{s\epsilon\rho_w V_m}{m_{dry}} \tag{A.46}$$

The conductivity is calculated using Eq. (A.45) [38]. Physical parameters of the membrane are obtained from NafionXL datasheet [54].

Appendix B. Model simulation procedure

The model simulation method has been implemented sequentially. The complete model is divided into different sub-models, and each model is simulated independently, feeding the boundary variables to the next model or the next step of the simulation. This procedure allows the validation of each model individually. The complete integrated model simulations reduce the overall computational complexity.

The flow-chart of the model simulation method procedure is shown in Fig. B.15. The simulation procedure is divided into six main subgroups, five within the solver loop and one out of the loop for configuration.

1. *Outside the loop*:

   Initialization: This group is set outside the simulation loop. In this section, the channel geometry, the membrane size, the meshes of spatial discretization setup of MLM and GDLs, and operating parameters are configured.

2. *In the loop*:

   (a) Updating cell operation setup: The parameters of operation setup, such as gas pressures, RHs, or injected liquid water, are updated beginning of each step.

   (b) Channel solver: The pressure drop due to reactants consumption, the relative humidity, and the movement of droplets in the channels are calculated.

   (c) Water balance: The water balance between the channel and the GDL is calculated. The evaporation and condensation, droplet re-absorption, and the relative humidity variation in the channel are evaluated.

   (d) MEA solver: The liquid water and gas diffusion inside the GDL, the electrochemical reactions, and the membrane water balance are computed for each spatial point of the cell.

   (e) Save and plot data: The data results of the simulation cycle are saved and plotted. This stage is not performed at every time step since it yields a significant overall simulation delay.

Appendix C. Supplementary data

Supplementary material related to this article can be found online at https://doi.org/10.1016/j.apenergy.2024.123234.

References

[1] Organization WH. COP26 special report on climate change and health: The health argument for climate action. World Health Organization; 2021, p. viii, 71.

[2] Mayur M, Gerard M, Schott P, Bessler W. Lifetime prediction of a polymer electrolyte membrane fuel cell under automotive load cycling using a physically-based catalyst degradation model. Energies 2018;11:2054.

[3] Ionescu V. Simulating the effect of gas channel geometry on PEM fuel cell performance by finite element method. Procedia Technol 2016;22:713–9.

[4] Yang WJ, Wang HY, Kim YB. Channel geometry optimization using a 2D fuel cell model and its verification for a polymer electrolyte membrane fuel cell. Int J Hydrog Energy 2014;39:9430–9.

[5] Steinbrenner JE, Lee EO, Hidrovo CH, Eaton JK, Goodson KE. Impact of channel geometry on two-phase flow in fuel cell microchannels. J Power Sources 2011;196:5012–20.

[6] Wang Y, Wang S, Liu S, Li H, Zhu K. Optimization of reactants relative humidity for high performance of polymer electrolyte membrane fuel cells with co-flow and counter-flow configurations. Energy Convers Manage 2020;205:112369.

[7] Morin A, Xu F, Gebel G, Diat O. Influence of PEMFC gas flow configuration on performance and water distribution studied by SANS: Evidence of the effect of gravity. Int J Hydrog Energy 2011;36:3096–109.

[8] de Cantabria U. Oscillation of PEFC under low cathode humidification: Effect of gravitation and bipolar plate design. ECS Electrochem Soc 2013.

[9] Zeroual M, Moussa HB, Tamerabet M. Effect of gas flow velocity in the channels of consumption reactants in a fuel cell type (PEMFC). Energy Procedia 2012;18:317–26.

[10] Pucheng P, Li Y, Xu H, Wu Z. A review on water fault diagnosis of PEMFC associated with the pressure drop. Appl Energy 2016;173:366–85.

[11] Jeon DH, Kim KN, Baek SM, Nam JH. The effect of relative humidity of the cathode on the performance and the uniformity of PEM fuel cells. Int J Hydrog Energy 2011;36:12499–511.

[12] Jamalabadi M, Ghasemi M, Alamian R, Afshare E, Wongwises S, Rashidi M, et al. A 3D simulation of single-channel high-temperature polymer exchange membrane fuel cell performances. Appl Sci 2019;9:1–17.

[13] Pan W, Chen X, Wang F, Dai G. Mass transfer enhancement of PEM fuel cells with optimized flow channel dimensions. Int J Hydrog Energy 2020.

[14] Zhong D, Lin R, Jiang Z, Zhu Y, Liu D, Cai X, et al. Low temperature durability and consistency analysis of proton exchange membrane fuel cell stack based on comprehensive characterizations. Appl Energy 2020;264:114626.

[15] Garofalo M. Water breakthrough behavior and GDL degradation mechanisms in a PEM fuel cell. RIT Sch Works 2012.

[16] Jung JH, Yoo SJ, Kim H-J, Jang JH, Nam SW, Cho EA. Degradation of polymer electrolyte membrane fuel cell under pressure cycle. ECS Meet Abstr 2014;MA2014-02(21):1151.

[17] García-Salaberri PA, Vera M, Zaera R. Nonlinear orthotropic model of the inhomogeneous assembly compression of PEM fuel cell gas diffusion layers. Int J Hydrog Energy 2011;36(18):11856–70.

[18] Tang Y, Kusoglu A, Karlsson AM, Santare MH, Cleghorn S, Johnson WB. Mechanical properties of a reinforced composite polymer electrolyte membrane and its simulated performance in PEM fuel cells. J Power Sources 2008;175(2):817–25.

[19] Sanchez DG, Ruiu T, Biswas I, Schulze M, Helmly S, Friedrich KA. Local impact of humidification on degradation in polymer electrolyte fuel cells. J Power Sources 2017;352:42–55.

[20] Lochner T, Hallitzky L, Perchthaler M, Obermaier M, Sabawa J, Enz S, et al. Local degradation effects in automotive size membrane electrode assemblies under realistic operating conditions. Appl Energy 2020;260:114291.

[21] Garcia D, Ruiu T, Friedrich K, Sanchez-Monreal J, Vera M. Analysis of the influence of temperature and gas humidity on the performance stability of polymer electrolyte membrane fuel cells. J Electrochem Soc 2015;163:F150.

[22] Dubau L, Castanheira L, Maillard F, Chatenet M, Lottin O, Gaël M, et al. A review of PEM fuel cell durability: Materials degradation, local heterogeneities of aging and possible mitigation strategies. Wiley Interdiscip Rev Energy Environ 2014;3:540–60.

[23] Wu J, Yuan XZ, Martin JJ, Wang H, Zhang J, Shen J, et al. A review of PEM fuel cell durability: Degradation mechanisms and mitigation strategies. J Power Sources 2008;184:104–19.

[24] Bruijin F, Dam VA, Janssen F. Review: Durability and degradation issues of PEM fuel cell components. Fuel Cells 2008;8:3–22.

[25] Weydahl H. Dynamic behaviour of fuel cells (Ph.D. thesis), 2006.

[26] Ehlinger VM, Crothers AR, Kusoglu A, Weber AZ. Modeling proton-exchange-membrane fuel cell performance degradation tradeoffs with chemical scavengers. J Phys Energy 2020;2.

[27] Muthukumar M, Karthikeyan P, Vairavel M, Loganathan C, Praveenkumar S, Kumar APS. Numerical studies on PEM fuel cell with different landing to channel width of flow channel. Procedia Eng 2014;97:1534–42.

[28] Liu Y, Gao J, Wang N, Yao S. Asymptotic analysis for the effects of anode inlet humidity on the fastest power attenuation single cell in a vehicle fuel cell stack. Appl Sci 2018;8(11):2307.

[29] Yan J, Zhou C, Rong Z, Wang H, Li H, Hu X. Simulation of the dynamic characteristics of a PEMFC system in fluctuating operating conditions. Energies 2020;13(14):1–17.

[30] Rizvandi OB, Yesilyurt S. A transient pseudo-3D model of the PEM fuel cell for the analysis of dead-ended anode and anode bleeding operation modes. Electrochim Acta 2019;324:134866.

[31] Gößling S, Nickig N, Bahr M. 2-D + 1-D PEM fuel cell model for fuel cell system simulations. Int J Hydrog Energy 2021;46(70):34874–82.

[32] Ferreira RB, Falcão DS, Oliveira VB, Pinto AM. 1D+3D two-phase flow numerical model of a proton exchange membrane fuel cell. Appl Energy 2017;203:474–95.

[33] Wang Y, Xu H, He W, Zhao Y, Wang X. Lattice Boltzmann simulation of the structural degradation of a gas diffusion layer for a proton exchange membrane fuel cell. J Power Sources 2023;556:232452.

[34] Bao N, Zhou Y, Jiao K, Yin Y, Du Q, Chen J. Effect of gas diffusion layer deformation on liquid water transport in proton exchange membrane fuel cell. Eng Appl Comput Fluid Mech 2014;8:26–43.

[35] Lindstrom M, Wetton B. A comparison of fick and Maxwell–Stefan diffusion formulations in PEMFC cathode gas diffusion layers. Heat Mass Transf 2013;53:205–12.

[36] Rakesh N, Shaneeth M, Jayaraj S. One dimensional modelling of oxygen diffusion in a gas diffusion layer of PEM fuel cell. In: International conference on green technologies. 2012, p. 340–2.

[37] Aminnia N, Shateri M, Torabi F. Modeling of two-phase flow in the cathode gas diffusion layer to investigate its effects on a PEM fuel cell. In: 3rd hydrogen and fuel cell conference. 2015.

[38] Yin C, Li J, Zhou Y, Zhang H, Fang P, He C. Phase separation and development of proton transport pathways in metal oxide nanoparticle/nafion composite membranes during water uptake. J Phys Chem A 2018;122:9710–7.

[39] Hyun-il K, Cho CY, Nam JH, Shin D, Chung T-Y. A simple dynamic model for polymer electrolyte membrane fuel cell (PEMFC) power modules: Parameter estimation and model prediction. Int J Hydrog Energy 2010;35:3656–63.

[40] Jaruwasupant N, Khunatorn Y. Effects of difference flow channel designs on proton exchange membrane fuel cell using 3-D model. Energy Procedia 2011;9:326–37.

[41] Hu K, Zhao P, Wang S, Wang Y. Three-dimensional multiphase simulation of a partially narrowed flow field configuration for a high-performance polymer electrolyte membrane fuel cell. Appl Therm Eng 2023;223:119986.

[42] Esposito A, Pianese C, Guezennec YG. Coupled modeling of water transport and air-droplet interaction in the electrode of a proton exchange membrane fuel cell. J Power Sources 2010;195:4149–59.

[43] Jarauta A, Secanell M, Pons-Prats J, Ryzhakov P, Idelsohn SR, Oñate E. A semi-analytical model for droplet dynamics on the GDL surface of a PEFC electrode. Int J Hydrog Energy 2015;40:5375–83.

[44] Bao Z, Niu Z, Jiao K. Gas distribution and droplet removal of metal foam flow field for proton exchange membrane fuel cells. Appl Energy 2020;280:116011.

[45] Zhang G, Fan L, Sun J, Jiao K. A 3D model of PEMFC considering detailed multiphase flow and anisotropic transport properties. Int J Heat Mass Transfer 2017;115:714–24.

[46] Sarmiento-Carnevali M, Serra M, Batlle C. Distributed parameter model-based control of water activity and concentration of reactants in a polymer electrolyte membrane fuel cell. Int J Hydrog Energy 2017;42:26389–407.

[47] Ghorbani B, Vijayaraghavan K. 3D and simplified pseudo-2D modeling of single cell of a high temperature solid oxide fuel cell to be used for online control strategies. Int J Hydrog Energy 2018;43:9733–48.

[48] Macedo-Valencia J, Sierra JM, Figueroa-Ramírez SJ, Díaz SE, Meza M. 3D CFD modeling of a PEM fuel cell stack. Int J Hydrog Energy 2016;41:23425–33.

[49] Culubret S, Rubio MA, Sanchez DG, Urquia A. Dynamic modeling of the effect of water management on polymer electrolyte fuel cells performance. Int J Hydrog Energy 2020;45:5710–22.

[50] Arabí AJ. Analysis of droplet dynamics on the GDL surface of a PEM fuel cell cathode. 2013.

[51] Schillberg CH, Kandlikar SG. A review of models for water droplet detachment from the gas diffusion layer-gas flow channel interface in PEMFCs. In: International conference on nanochannels, microchannels, and minichannels, vol. 4272X, 2007, p. 1–12.

[52] Springer TE, Zawodzinski TA, Gottesfeld S. Polymer electrolyte fuel cell model. J Electrochem Soc 1991;138(8):2334–42.

[53] García-Salaberri PA, Sánchez DG, Boillat P, Vera M, Friedrich KA. Hydration and dehydration cycles in polymer electrolyte fuel cells operated with wet anode and dry cathode feed: A neutron imaging and modeling study. J Power Sources 2017;359:634–55.

[54] NafionXL specifications datasheet, URL https://www.fuelcellsetc.com/store/NXL. [Accessed 22 December 2020].

[55] Donnarumma D, Tomaiuolo G, Caserta S, Gizaw Y, Guido S. Water evaporation from porous media by dynamic vapor sorption. Colloids Surf A 2015;480:159–64.

[56] Stampino PG, Molina D, Omati L, Turri S, Levi M, Cristiani C, et al. Surface treatments with perfluoropolyether derivatives for the hydrophobization of gas diffusion layers for PEM fuel cells. J Power Sources 2011;196:7645–8.

[57] Pasaogullari U, Wang CY. Liquid water transport in gas diffusion layer of polymer electrolyte fuel cells. J Electrochem Soc 2004;151:A399.

[58] Cheema TA, Kim GM, Lee CY, Kwak MK, Kim HB, Park CW. Effects of composite porous gas-diffusion layers on performance of proton exchange membrane fuel cell. Int J Precis Eng Manuf Green Technol 2014;1:305–12.

[59] Hussaini IS, Wang CY. Measurement of relative permeability of fuel cell diffusion media. J Power Sources 2010;195:3830–40.

[60] Benziger J, Nehlsen J, Blackwell D, Brennan T, Itescu J. Water flow in the gas diffusion layer of PEM fuel cells. J Memb Sci 2005;261:98–106.

[61] Whitaker S. Flow in porous media I: A theoretical derivation of Darcy's law. Transp Porous Media 1986;1:3–25.

[62] Santamaria AD, Das PK, MacDonald JC, Weber AZ. Liquid-water interactions with gas-diffusion-layer surfaces. J Electrochem Soc 2014;161:F1184–93.

[63] Das PK, Santamaria AD, Weber AZ. Interactions between liquid-water and gas-diffusion layers in polymer-electrolyte fuel cells. Procedia Eng 2015;105:751–6.

[64] Chaudhary S, Sachan VK, Bhattacharya PK. Two dimensional modelling of water uptake in proton exchange membrane fuel cell. Int J Hydrog Energy 2014;39:17802–18.

[65] Gad AAM, Abd-Elaal AM. Practical guidelines for a reliability-based design of building water supply systems. Urban Water J 2015;13(2):1–14.

[66] Chapter 3: Fuel cell reaction kinetics, Wiley, 2016, pp. 77–116.